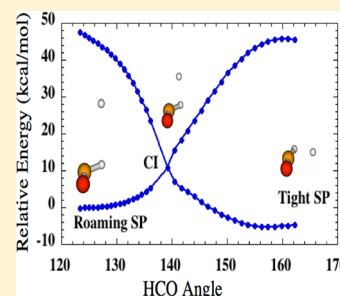


Separability of Tight and Roaming Pathways to Molecular Decomposition

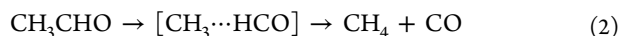
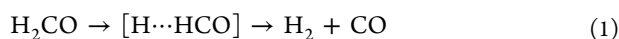
Lawrence B. Harding,^{*,†} Stephen J. Klippenstein,[†] and Ahren W. Jasper[‡][†]Chemical Sciences and Engineering Division, Argonne National Laboratory, Argonne, Illinois 60439, United States[‡]Combustion Research Facility, Sandia National Laboratories, Livermore, California 94551, United States

ABSTRACT: Recent studies have questioned the separability of the tight and roaming mechanisms to molecular decomposition. We explore this issue for a variety of reactions including $\text{MgH}_2 \rightarrow \text{Mg} + \text{H}_2$, $\text{NCN} \rightarrow \text{CNN}$, $\text{H}_2\text{CO} \rightarrow \text{H}_2 + \text{CO}$, $\text{CH}_3\text{CHO} \rightarrow \text{CH}_4 + \text{CO}$, and $\text{HNNOH} \rightarrow \text{N}_2 + \text{H}_2\text{O}$. Our analysis focuses on the role of second-order saddle points in defining global dividing surfaces that encompass both tight and roaming first-order saddle points. The second-order saddle points define an energetic criterion for separability of the two mechanisms. Furthermore, plots of the differential contribution to the reactive flux along paths connecting the first- and second-order saddle points provide a dynamic criterion for separability. The minimum in the differential reactive flux in the neighborhood of the second-order saddle point plays the role of a mechanism divider, with the presence of a strong minimum indicating that the roaming and tight mechanisms are dynamically distinct. We show that the mechanism divider is often, but not always, associated with a second-order saddle point. For the formaldehyde and acetaldehyde reactions, we find that the minimum energy geometry on a conical intersection is associated with the mechanism divider for the tight and roaming processes. For HNNOH , we again find that the roaming and tight processes are dynamically separable but we find no intrinsic feature of the potential energy surface associated with the mechanism divider. Overall, our calculations suggest that roaming and tight mechanisms are generally separable over broad ranges of energy covering most kinetically relevant regimes.



I. INTRODUCTION

In roaming radical reactions^{1–3} one bond in a molecule becomes greatly extended, typically to more than twice the equilibrium bond length and then, before the nascent radicals completely separate, they reorient and react, often by disproportionation. The two most thoroughly studied roaming radical reactions are the dissociations of formaldehyde^{4–6} and acetaldehyde,^{7–10}



Roaming saddle points for both of these reactions have been reported¹¹ in which one bond (CH in the case of H_2CO and CC in the case of CH_3CHO) is greatly elongated. These reactions also have tight saddle points with compact three-center structures connecting the same sets of reactants and products. The reaction paths associated with the roaming and tight saddle points result in two distinct mechanisms for the same net reaction, and experimental evidence for the presence of two mechanisms played a crucial role in identifying the existence of the roaming radical mechanism.^{1,4,7}

Roaming radical pathways may also provide alternative reaction paths for isomerization.¹² This can happen when the reorientation of the incipient radicals leads to an addition reaction rather than an abstraction reaction. This roaming radical induced isomerization is especially likely when the nascent radicals include at least one resonantly stabilized radical

with significant radical character at multiple sites. After a long-range reorientation of the two radicals, readdition can occur at a different site. For ion–molecule reactions, roaming pathways are even more significant due to the increased strength of the long-range interactions and, for this reason, have long been known to be important.^{13,14} Roaming pathways also exist for radical decompositions^{15,16} in which a nascent radical and molecule are formed, reorient, and react. However, the roaming contributions here are often reduced, due to the presence of significant barriers for the final radical–molecule reactions.

Dynamical and statistical theoretical models for treating the kinetics of roaming radical reactions were recently presented in refs 17 and 12, respectively. A key assumption in both of these models is that the contributions from the roaming and tight reaction pathways are separable. As discussed below, the proper transition state dividing surface is always a global surface that includes contributions from every competing pathway connecting a given set of reactants to products. In practice, it is often convenient to approximate this global dividing surface as consisting of separate contributions from the different processes. Within this approximation one may then use different dynamical methods to characterize each process. In our statistical and dynamical treatments of roaming, for example, the roaming radical pathways were modeled by

Received: April 13, 2012

Revised: June 4, 2012

Published: June 6, 2012



considering the long-range reorientational dynamics of the two incipient radicals approximated as rigid bodies. Meanwhile, the dynamics of the tight transition states were calculated independently using variational transition state theory (TST) and the rigid rotor–harmonic oscillator (RRHO) approximation.

The goal of this paper is to address the question of the validity of the presumed separation of the roaming and tight pathways for roaming radical reactions. We emphasize the importance of considering *dynamic* separability and not simply energetic separability. We do so through illustrative studies of global transition state dividing surfaces for some representative cases of roaming radical reactions. The results and framework we present are also relevant to the more general question of separability for any reaction having multiple pathways.¹⁸

This paper is organized into five sections. In the first section we briefly review key elements of TST, define what we mean by global dividing surfaces, including how one might define optimal global dividing surfaces, and finally discuss how one can use these surfaces to address this question of separability. The case of a transition state dividing surface with multiple torsional minima is used to illustrate the importance of the second-order saddle point to the determination of optimal global dividing surfaces. The energy of the second-order saddle point plays a key role in the separability issue.

Next we consider two simple examples of triatomic reactions with competing pathways. The first is the dissociation of MgH_2 to $\text{Mg} + \text{H}_2$ and the second is the isomerization of NCN to CNN . In both cases there are two competing pathways connecting the same sets of reactants and products, one having a tight saddle point and one with a long-range roaming saddle point. The dimensionality of these two systems is sufficiently small that one can readily define global dividing surfaces that include both saddle points and address the question of separability on these global dividing surfaces. A key conclusion here is that in each case there exists a second-order saddle point on the global dividing surface. The energy of the second-order saddle point provides a valid indication of the energetic separability of fluxes associated with the two, first-order saddle points. Meanwhile, the differential contribution to the reactive flux at the second-order saddle point provides a valuable indication of the dynamic separability of the two pathways. This differential reactive flux may be evaluated via either trajectory simulations or statistical theories. Here, we choose to use statistical theories.

We then consider the more complicated formaldehyde and acetaldehyde decompositions, which have been the focus of many earlier theoretical studies. For these reactions, we again look for second-order saddle points but instead find conical intersections separating the two reaction paths. We map out the connections between the conical intersections and the two first-order saddle points, and we find that the conical intersections play an analogous role in determining the separability of the two pathways as the second-order saddle points played for the triatomic examples.

Finally, we conclude with a discussion of the decomposition of HNNOH , which is a key intermediate in the $\text{NH}_2 + \text{NO}$ reaction of importance in thermal de- NO_x . In this case, the long-range attractions are so strong that there do not appear to be separate roaming and tight saddle points, although we find evidence that a roaming-type process does play a role as a sizable anharmonicity in one of the bound modes of the tight saddle point. Interestingly, the differential contributions to the

reactive flux indicate that even for this case the roaming and tight mechanisms are dynamically separable.

II. TRANSITION STATE THEORY, SADDLE POINTS, AND GLOBAL DIVIDING SURFACES

II.A. Transition State Theory Background. There have been many excellent presentations of the fundamental concepts of TST.^{19–22} Here we review those aspects of TST relevant to the question of separability.

The concept of a reaction is meaningful only when the reactants and products can be identified as distinct from one another in some way. For chemical reactions, reactants and products differ in their bonding arrangements, and these different bonding arrangements are associated with distinct, localized regions of configuration space. For such reactions, it necessarily follows that one can identify an $n-1$ -dimensional (hyper)surface through configuration space that completely separates reactants from products, where n is the number of internal degrees of freedom of the system. By construction, any dynamical path in configuration space that connects reactant configurations to product configurations must pass through such a dividing surface at least once. There are an infinite number of such dividing surfaces, differing from one another in their geometrical parameters. The only restriction on the members of this family of dividing surfaces is that each dividing surface must completely separate reactants from products.

The classical flux through a dividing surface for a microcanonical distribution of states at fixed total energy, E , is proportional to the classical state count, N_E , commonly expressed as²⁰

$$N_E^{(s)} = \frac{1}{h^{n-1}} \int_{q^{(s)}} d\mathbf{Q} \int d\mathbf{P}^{(s)} \Theta(E - H) \quad (3)$$

where the n coordinates \mathbf{Q} are restricted to the $n-1$ -dimensional dividing surface $q^{(s)}$, $\mathbf{P}^{(s)}$ are the conjugate momenta for motion on $q^{(s)}$, s is an index that labels the dividing surface, H is the total energy, and Θ is the Heaviside step function. The classical state count for any dividing surface s will, in general, be greater than the net reactive flux N_E^\ddagger due to some reactive trajectories being overcounted as they cross the dividing surface more than once on their way from reactants to products and due to some nonreactive trajectories being counted as they pass through the dividing surface, but later head back to reactants. This observation is the source of the variational principle, which states that because $N_E^{(s)} \geq N_E^\ddagger$ for any s , minimizing the flux with respect to the geometric parameters of the dividing surface necessarily improves the rate. Furthermore, one can show that the exact classical rate is proportional to the fully variationally optimized flux N_E^\ddagger , but only when the momenta are included in the definition of the dividing surface. Several elegant proofs of this fundamental law of classical mechanics have been given over the decades by Wigner,²³ Keck,²⁴ Pechukas and Pollak,²⁵ Miller,²⁶ and others. The fully variationally optimized dividing surface is called the transition state dividing surface or simply the transition state.

The variational principle is the cornerstone of all practical implementations of TST, where, in place of a complete optimization of the dividing surfaces to obtain the exact rate, one considers limited minimizations of the reactive flux within a restricted set of dividing surfaces to obtain an upper bound to the rate. The geometric prescription for the dividing surfaces and the choice of how to count states on the dividing surfaces

determines the accuracy of these TST predictions. Although TST is formally a classical theory, useful modern applications generally employ ad hoc quantum mechanical corrections involving the replacement of the classical state counts with quantum state counts and corrections for dynamical tunneling through and reflection from the barrier.

One can also formulate a canonical (thermal) TST rate expression and a canonical version of the variational principle, where the information at the transition state takes the form of a temperature dependent pseudopartition function $Q_T^{(s)}$ evaluated for the $n - 1$ degrees of freedom of the dividing surface²⁰

$$Q_T^{(s)} = \frac{1}{h^{n-1}} \int_{q^{(s)}} d\mathbf{Q} \int d\mathbf{P}^{(s)} \exp(-\beta H) \quad (4)$$

The pseudopartition function $Q_T^{(s)}$ is again minimized with respect to geometric parameters of the dividing surface to improve the predicted rate coefficient. Alternatively, more accurate TST estimates are obtained by accounting for the conservation of total angular momentum, J , and focusing on E and J resolved state counts during the variational optimizations.

We emphasize that, whenever a description in terms of rate constants is appropriate, it is always possible—at least formally—to define a valid transition state dividing surface that completely separates reactants from products, independent of the number or variety of competing reaction paths. This claim relies solely upon the necessary $n-1$ -dimensional geometric separation of the localized reactant and product configurations associated with chemical reactions. Generally, this reactant–product separation fails only at high energies (or temperatures) where the transformation between them becomes so rapid that the distinction between the reactants and products is blurred.²⁷ We note that, for some systems, particularly those with intermediate wells, the system may pass through more than one transition state dividing surface *in series* on its way from reactants to products.^{28,29} Furthermore, some processes may be poorly described by the stochastic/equilibrium assumptions inherent in TST.^{30,31} We do not consider these complications further.

II.B. First-Order Saddle Points. The first-order saddle point, which is a single geometry characterized as having zero potential gradient and one negative Hessian eigenvalue, plays a key role in TST. Unfortunately, this saddle point is often conflated with the transition state, which, as discussed above, is an $n-1$ -dimensional hypersurface. As one approaches the limit of zero temperature, the variationally optimized transition state dividing surface moves toward and ultimately contains the first-order saddle point,³² and saddle points are therefore often useful in defining transition state dividing surfaces. Nevertheless, the saddle point and transition state are fundamentally different geometric objects.

To define a dividing surface from a saddle point, one needs to make additional choices. One particularly useful choice is to define the dividing surface as passing through the first-order saddle point, perpendicular to the normal mode vector associated with the imaginary frequency. This prescription is designed to yield the minimal state count for a quadratic expansion of the potential about the saddle point. As such, it generally yields accurate rate predictions at near-threshold energies. However, with increasing energy, additional terms in the potential become important. The optimal dividing surfaces then tend to be increasingly displaced from the saddle point and also may not be oriented perpendicularly to the direction of the imaginary frequency's normal mode vector. Furthermore,

for quantum state counts, vibrational zero-point energies can lead to displacements even in the zero-temperature limit.

One useful scheme for generating a series of candidate dividing surfaces for the variational TST minimization is to follow the intrinsic reaction coordinate (IRC) downhill from the saddle point. Coordinates along this path may be labeled by the reaction coordinate s , which describes the mass-scaled distance along the IRC from the saddle point toward either the reactants (negative s) or the products (positive s). Along the IRC, but displaced from the saddle point, one can define useful dividing surfaces as perpendicular to the nuclear gradient. Alternatively one can follow a minimum energy path (MEP) from the saddle point to reactants and products. In following an MEP, one first chooses a particular internal coordinate, which ideally will have high overlap with the reaction coordinate. Then, for a range of different fixed values of this distinguished coordinate, one optimizes to a minimum in the remaining $n - 1$ degrees of freedom. A family of dividing surfaces can then be defined along the MEP in the same way as is done for an IRC. The utility of a given MEP depends greatly on the choice of the distinguished coordinate and how smoothly it connects reactants, saddle point, and products. For poor choices of a distinguished coordinate the MEP is not guaranteed to pass through the saddle point.

II.C. Counting States. The evaluation of eqs 3 and 4 can in principle be performed exactly, although in practice one often uses the harmonic oscillator and rigid rotor approximations. Within the RRHO approximations, one then variationally optimizes $N_E^{(s)}$ and $Q_T^{(s)}$ with respect to s and other choices of the dividing surface, as discussed above. Here, we highlight three characteristics of the potential energy surface along the global dividing surface that influence the state count $N_E^{(s)}$ and pseudopartition function $Q_T^{(s)}$: (1) the potential energy along the dividing surface, (2) the frequencies perpendicular to the reaction coordinate, and (3) the total volume of the dividing surface. These considerations controlling the state count are of course not independent of one another, and the best variational dividing surface is the best *compromise* of maximizing the potential energy along the dividing surface, maximizing the frequencies perpendicular to the reaction coordinate, and minimizing the volume of the dividing surface. By definition, this compromise minimizes dynamical recrossing. We also highlight one key dynamical criterion: namely that, near threshold, the dividing surface that is perpendicular to the reaction coordinate and passes through the saddle point minimizes dynamical recrossing.

II.D. Global Dividing Surfaces, the Second-Order Saddle Point, and Mechanism Separability. In general, there may be multiple first-order saddle points connecting a given chemical species to a given product, or more generally to a variety of products. The proper implementation of TST then requires a global dividing surface completely separating the reactants from each of these products via each of the pathways and allowing for passage through the neighborhood of each saddle point. Qualitatively, one expects that this global dividing surface should consist of a union of segments that are locally optimal for the regions about each of the saddle points. Often, one presumes that the local segments are independent and that the total reactive flux can simply be written as the sum of the fluxes for TS dividing surfaces optimized separately for each segment of the dividing surface. In this work, we wish to proceed beyond this typical assumption and explicitly explore some global dividing surfaces for several roaming radical

reactions. As a prelude to this, we consider the simpler case of a dissociation reaction with a torsion, where it is relatively easy to comprehend the nature of the optimal global dividing surface.

For many dissociation reactions, there are two or more saddle points that differ principally only in their torsional configurations. Furthermore, there are generally second-order saddle points, with zero gradients and two negative eigenvalues for the Hessian, separating these first-order saddle points. Such reactions provide a particularly simple case for considering the global dividing surface. Consider, for example, the two-dimensional representation in Figure 1 of the potential energy

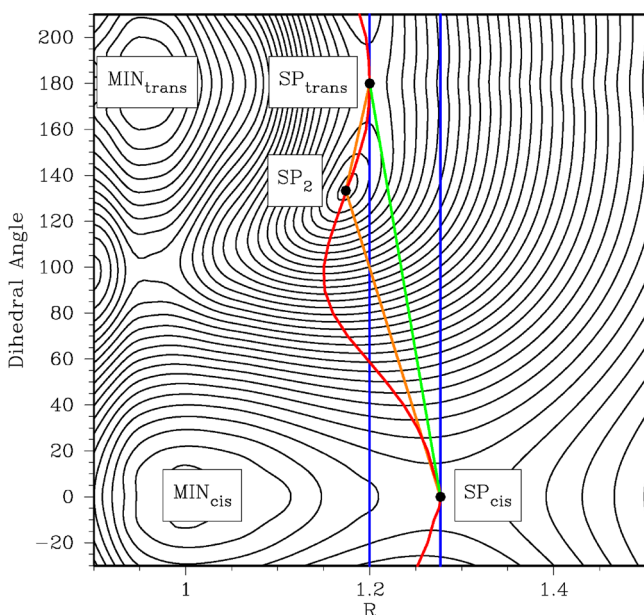


Figure 1. Contour plot for the interaction of an H atom with a rigid CO_2 molecule, with the CO_2 molecule held fixed at its geometry for the cis first-order saddle point. R is the OH distance. The contour spacings are 1 kcal/mol. The blue, green, orange, and red lines denote the Model 0, 2, 3 and SPP transition state dividing surfaces. Note that the complete global dividing surfaces include symmetrical extensions of these lines to 360° .

surface for the decomposition of HOCO into $\text{H} + \text{CO}_2$. For this reaction there are two first-order saddle points corresponding to cis (SP_{cis}) and trans (SP_{trans}) orientations of the HOCO dihedral angle. At both of these saddle points, R (the O–H distance) closely describes the reaction coordinate. There is also a second-order saddle point (SP_2) that lies between the two first-order saddle points.

There are various procedures one could employ in generating a global dividing surface for the HOCO decomposition. A particularly simple approach (Model 0) involves the extrapolation of the optimal near-threshold local dividing surface at the cis saddle point to cover the full torsional range. (The numbered models discussed throughout this section are presented in more detail in the Appendix.) As discussed above, the optimal dividing surface at near threshold energies is perpendicular to the reaction coordinate and passes through the saddle point, as shown by the blue line in Figure 1. Note that this dividing surface is valid as it completely separates the reactants from the products. However, it passes near the trans saddle point at a lower potential energy than the energy of the trans saddle point, and one may therefore expect significant recrossing in this region and an overestimate of the predicted

rate coefficient for this choice of global dividing surface. Alternatively, the corresponding local trans dividing surface could also be used (i.e., a dividing surface perpendicular to R and passing through SP_{trans}). This choice would be more suitable near SP_{trans} but is not suitable near SP_{cis} . Either of these choices for the global dividing surface would lead to an overprediction of the reaction rate.

Another approach (Model 2) would involve the surface connecting the two first-order saddle points (e.g., linearly), as illustrated by the green line. This choice may appear to be a clear improvement over Model 0 as it increases the potential energy along the global dividing surface. However, this surface is not locally perpendicular to the reaction coordinate at either of the saddle points. This defect of linear interpolations is general and may lead to recrossing near both of the saddle points, particularly at low energies. Instead of linearly interpolating, one could interpolate between the two blue dividing surfaces in some other way such that the resulting global surface was locally perpendicular to the reaction coordinates for each of the saddle points. The resulting global dividing surface would feature reduced dynamical recrossing near each of the saddle points but would necessarily feature a larger volume.

Notably, these first two models make no use of any information about the second-order saddle point and are generated from the data for the first-order saddle points alone. Global dividing surfaces that pass through the second-order saddle point might be expected to yield more optimal dividing surfaces due to reduced recrossing in the vicinity of the second-order saddle point. The simplest such global dividing surface (Model 3) linearly connects the second-order saddle point to the two first-order saddle points and is denoted with the pair of orange lines in Figure 1. Again, one could attempt to improve this model by forcing the global dividing surface to be perpendicular to the reaction coordinate near the saddle points. Note that a dividing surface defined by Model 3 will in general have a larger volume than that defined by Model 2. This increase in volume is likely more than offset by the increase in the potential energy along the global dividing surface.

A final model is obtained by performing a constrained saddle point search in R for each torsional angle. Notably, the red line connecting these distinguished coordinate saddle points passes through the first- and second-order saddle points and is essentially parallel to the locally optimal cis and trans dividing surfaces in the neighborhood of the first-order saddle points. We label this path, connecting the two first-order saddle points and the second-order saddle point, the saddle point path (SPP) in analogy with MEPs, which connect two minima through a first-order saddle point.

The potential energy values along the torsional coordinate are illustrated in Figure 2 for each of these model global dividing surfaces. As discussed above, one criterion for the optimal dividing surface is that it is likely to be the one with the most positive potential energies along the dividing surface. According to this criterion, the two Model 0 surfaces are clearly inadequate. The one based on the cis local surface has much lower potential values in the neighborhood of SP_{trans} than do the other models. Similarly, the one based on the trans local surface falls below that for the cis local surface in the neighborhood of SP_{cis} . Furthermore, they both fail to capture the high potential values near SP_2 . The Model 2 surface similarly misses the high potential values near SP_2 . In contrast,

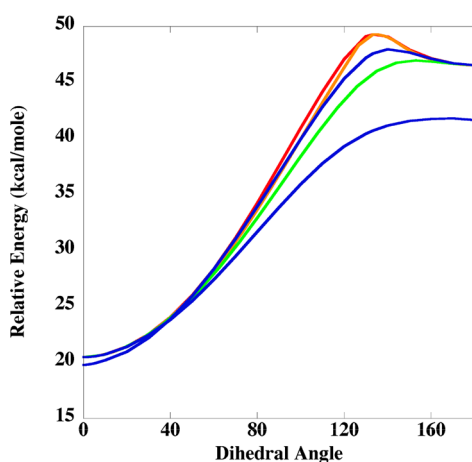


Figure 2. Plot of the potential energy along the model dividing surfaces. The line colors match those in Figure 1. Blue denotes Model 0, green Model 2, orange Model 3, and red the SPP.

the SPP and Model 3 surfaces are both higher than the Model 0 and 2 surfaces throughout and particularly near SP_2 .

It might seem like the SPP model should always lead to a higher energy dividing surface than the other models. This expectation is correct in our simple, two-dimensional, $H + CO_2$ example because, once we have fixed the distinguished coordinate, there is only one coordinate left and we are maximizing the energy with respect to that coordinate. It will not be true in general for higher dimensional problems where each point on the SPP comes from a multidimensional saddle point optimization rather than a simple energy maximization. We have in fact found examples where linear interpolations between two first-order saddle points lead to barriers that are higher than the true second-order saddle point. However, these linear interpolations do not provide better dividing surfaces as the potential energy surface orthogonal to the interpolation coordinate now has minima that are lower than the corresponding point on the linear approximation to the SPP. In summary, linear interpolations between two saddle points will provide neither lower bounds nor upper bounds on the energetic separability of the two saddle points and do not provide improved global dividing surfaces even when their maximum lies higher than the second-order saddle point.

We emphasize that the utility of a given SPP will depend critically on the choice of the distinguished coordinate. For cases where a suitable distinguished coordinate can be found that leads to a SPP that smoothly connects the first- and second-order saddle points, we expect that the SPP will serve as a useful starting point for a fully, variationally optimized, global dividing surface. We note that Maronsson et al.³³ have recently reported a rigorous algorithm for following ridges between two first-order saddle points. These ridges can be considered as an analogue of the IRC, just as the distinguished coordinate SPP is the analogue of the MEP. This kind of approach may be necessary in cases where a suitable choice for a distinguished coordinate cannot be found.

The separability of two mechanisms is best defined in terms of the *dynamic* separability of the pathways, with the key question being whether or not there is some separation in phase space between trajectories that follow one mechanism as opposed to the other? The energy of the second-order saddle point, E_{SP_2} , defines an *energetic* separability for the two pathways. Below this energy the two pathways must be

dynamically distinct. Importantly, although energetic separability guarantees dynamic separability, the converse does not necessarily hold; i.e., the processes may be separable dynamically even if energetically they are not.

Notably, TST provides a means for directly examining the *dynamic* separability of the pathways. For a global dividing surface that spans both regions, one may consider the differential contribution to the flux through the global dividing surface as a function of the coordinate along some path, such as the SPP, that connects the first-order saddle points. This differential flux generally has a minimum in the neighborhood of the second-order saddle point. When the differential flux at this minimum is much less than that at the first-order saddle points, the two pathways are dynamically distinct. For concreteness, we label the $n-2$ -dimensional surface on which the differential flux has its minimum as the mechanism divider surface. The examples given below are used to further discuss and illustrate these separability issues.

In summary, the second-order saddle point is a key geometrical object for the determination of optimal global dividing surfaces. Its role in the exploration of global dividing surfaces is analogous to the role of the first-order saddle point in the determination of the local TS dividing surfaces. Global transition state dividing surfaces that include it are expected to provide a good first approximation to the optimal dividing surface. The Model 3 and SPP surfaces, which we and others³⁴ have been using to obtain torsionally global transition state dividing surfaces for a number of reactions, provide a good starting point for considering the appropriateness of the separation into independent sums of locally evaluated reactive fluxes. Importantly, the second-order saddle point provides a good first approximation to the location of the mechanism divider surface. Finally, we note that the usefulness of the second-order saddle point in determining separability relies upon it being an energy maximum in two coordinates and an energy minimum in the remaining coordinates. Another geometrical object that satisfies these criteria is the minimum energy point on a conical intersection. We will see below that for some systems the minimum energy point on a conical intersection does in fact play the role that the second-order saddle point played for HOCO.

We now illustrate the first- and second-order saddle points and the corresponding model global dividing surfaces for several examples of roaming radical reactions. We also delve into the question of transition state separability for each of these examples via considerations of the differential reactive flux for the mechanism divider surface.

III. TRIATOMIC EXAMPLES

III.A. MgH_2 . Recent quantum dynamics calculations by Takayanagi et al.³⁵ using an analytic surface by Li et al.³⁶ have shown that MgH_2 dissociates to $Mg + H_2$ via two distinct mechanisms, the first over a conventional, tight saddle point and the second via a roaming type mechanism. Indeed, their calculations suggest that the roaming mechanism is the dominant mechanism for formation of the $Mg + H_2$ products. A contour plot of the potential surface for this reaction is shown in Figure 3. Four stationary points are visible in this plot, the global minimum (collinear $HMgH$), the tight saddle point for dissociation to $Mg + H_2$, the roaming saddle point leading to the same products, and a second-order saddle point between the two first-order saddle points. (Note that for each of the saddle points there are symmetrically related stationary points

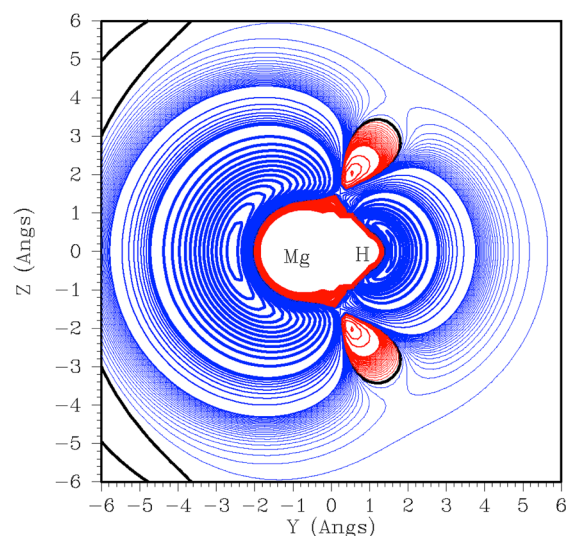


Figure 3. Contour plot for the interaction of an H atom with a rigid MgH radical. The blue contours denote attractive interactions, and the red denote repulsive interactions (relative to the MgH + H asymptotic energy). The contour spacings are 0.02 kcal/mol for the thinnest lines and 0.5 kcal/mol for the lines of medium thickness and 5.0 kcal/mol for the thickest contour lines. The MgH bond length for the rigid MgH fragment is 1.71 Å.

above and below the MgH axis.) The properties of the four stationary points are given in Table 1. The potential surface is qualitatively similar to that of formaldehyde in that the overall dissociation to Mg + H₂ is close to thermoneutral and the tight and roaming saddle points are also close to each other in energy. Also visible in Figure 3 is a very prominent, barrierless disproportionation pathway for the reaction MgH + H → Mg + H₂, again qualitatively similar to the H + HCO disproportionation path.

Although the geometries of the three saddle points are quite different, the HMgH angle, θ , varies by only 2° between the three saddle points, from 55.9° to 57.5°. Furthermore, the character of the normal mode vectors associated with the imaginary frequencies for the two first-order saddle points is predominantly an HMgH bend. A useful global dividing surface is therefore given by the constraint $\theta = \sim 56.5^\circ$. A better but more complicated dividing surface would be one in which for each value of R_{MgHa} and R_{MgHb} on the dividing surface θ is optimized to find the maximum energy. A plot of the potential on this dividing surface is shown in Figure 4. Although this plot is qualitatively reminiscent of a potential energy surface for A + BA → ABA → AB + A, the significance of this surface is quite different as we must consider the reactive flux moving through this surface rather than on it. In this plot then, the “minimum”

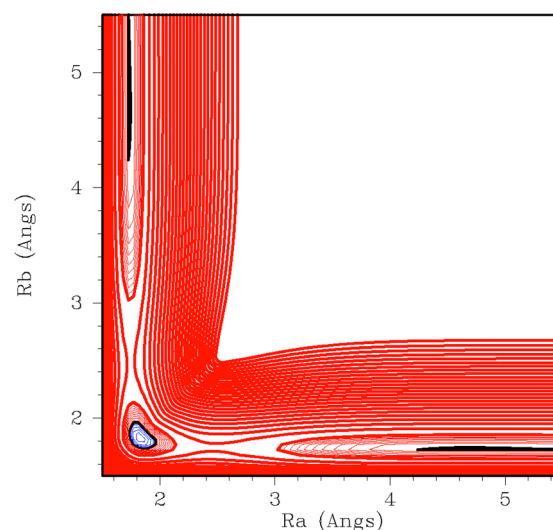


Figure 4. Contour plot of an optimized dividing surface for the reaction MgH₂ → Mg + H₂. At each point on this plot the angle θ is chosen to locally maximize the energy. The contour interval for the thick (thin) contours is 1.0 (0.1) kcal/mol. Other plotting conventions are as in Figure 3.

in the lower left is the tight saddle point and the entrance and exit channel “minima” correspond to the two equivalent roaming saddle points. The two equivalent “saddle points” in this plot, at (1.8,2.5) and (2.5,1.8), correspond to the second-order saddle points. From this plot then it is clear that the second-order saddle points provide a measure of the separability of the fluxes associated with the tight and roaming saddle points. If one is only interested in energies below that of the second-order saddle point, the tight and roaming fluxes may be treated independently for this choice of global dividing surface. At higher energies an accurate transition state theory treatment may require the use of a global dividing surface such as that shown in Figure 4.

For more complicated, higher-dimensional systems and for systems where the reaction coordinates for the competing processes differ significantly, it may be difficult to represent good global dividing surfaces as clearly as in Figure 4. However, the analysis for HMgH suggests that one can study separability by examining one-dimensional pathways connecting the first-order saddle points using the models discussed in section II.

From Figure 3 it is clear that one can define many pathways connecting the two first-order saddle points that exhibit no barrier separating these saddle points. We emphasize that these low energy pathways are irrelevant to the question of separability (either energetic or dynamic) as they are not on or near the optimal global dividing surface. Instead, and as

Table 1. (4E,6O)-CAS+1+2+QC/cc-pVQZ Geometries, Frequencies, and Energies of the Stationary Points on the MgH₂ Potential Surface

	MgH ₂	MgH + H	Mg + H ₂	tight SP	roaming SP	2nd-order SP
R_{MgH} (Å)	1.711	1.742		1.820	1.742, 4.69	1.743, 2.471
R_{HH} (Å)			0.74			
$\angle \text{H-Mg-H}$ (deg)	180			57.5	56.4	55.9
ω_1 (cm ⁻¹)	1628	1490	4398	1030	1491	1506
ω_2 (cm ⁻¹)	1601			532	36	1131i
ω_3 (cm ⁻¹)	441(x2)			3566i	73i	376i
energy (kcal/mol)	-72.65	0.00	-76.37	-0.60	-0.04	1.86

discussed in section II, one may address the question of separability by characterizing the potential energy surface near the ridge connecting the two first-order saddle points, i.e., near the SPP. For HMgH, the geometries of the two first-order saddle points differ significantly in only one internal coordinate (one of the MgH distances). This coordinate then is an ideal choice for a distinguished coordinate in an SPP calculation. Here, one MgH distance is kept fixed at each of a range of different values and for each choice of the fixed MgH distance the remaining two coordinates are optimized to a saddle point. A plot of the energy along this SPP is shown in Figure 5. The

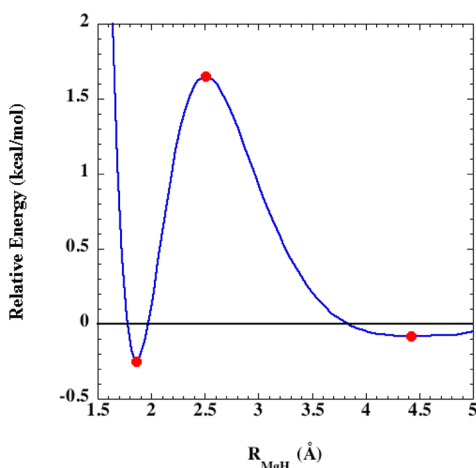


Figure 5. SPP for the dissociation of MgH_2 as a function of the one of the MgH distances. The solid red dots correspond to the first- and second-order saddle points.

three dots on this plot correspond to geometries and energies of the full-dimensional stationary points. The fact that these lie so close to our approximate ridge suggests that this one-dimensional path is a good representation of the global ridge separating reactants and products.

Having an approximate global transition state dividing surface (Figure 4) allows us to also investigate the question of dynamic separability in detail. In particular, we use the coordinate $\nu = r_{\text{MgH}_2} - r_{\text{MgH}_1}$ to denote the position along the SPP. We then evaluate the differential contribution to the number of available states at the transition state, $N' = dN/d\nu$, as a function of ν . This contribution is readily evaluated via integration over $u = r_{\text{MgH}_1} + r_{\text{MgH}_2}$ under the reasonable assumption that the SPP corresponds to fixed θ .³⁷ For simplicity, we restrict our considerations to a planar model but include fully anharmonic state counts within this model. Generalizations to a full three-dimensional model would increase the relative importance of the roaming contribution due its lower rotational constants but is not expected to affect the qualitative conclusions.

This ν dependent contribution to the transition state number of states is illustrated in Figure 6 for a range of energies. The minimum in each of the lines (i.e., the value for the mechanism divider surface) correlates with the location of the second-order saddle point. For excess energies of 2 kcal/mol and lower (relative to the $\text{MgH} + \text{H}$ asymptote) the tight and roaming transition states are completely separated with a 0 contribution in the neighborhood of the second-order saddle point. At 4 kcal/mol, which is 2.3 kcal/mol higher than the second-order saddle point, there is still a significant dynamic separation, as

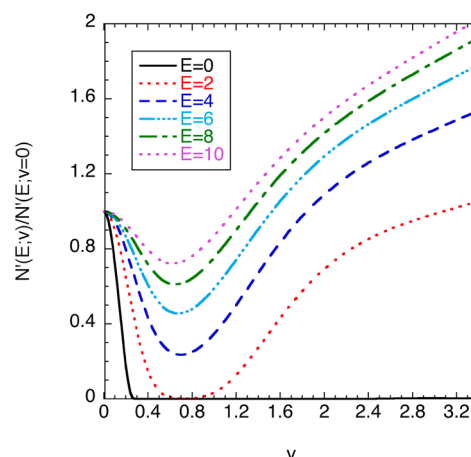


Figure 6. Plot of the differential contribution to the transition state number of states $N'(\nu)$ as a function of the SPP coordinate ν normalized by the differential contribution at the minimum in the potential for the global dividing surface ($\nu = 0$). The different lines denote the N' values for different energies in kcal/mol relative to $\text{MgH} + \text{H}$.

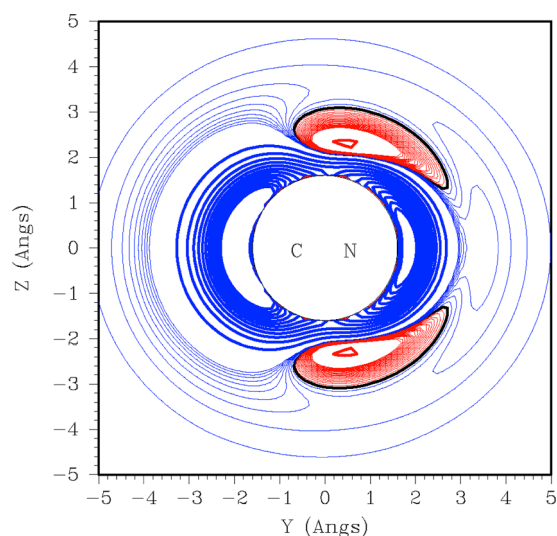
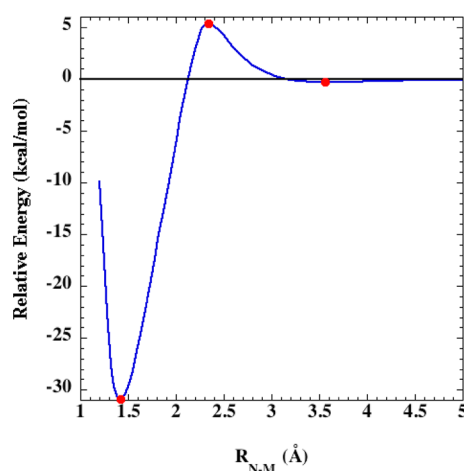
the contribution at the second-order saddle point is still only 20% of that at $\nu = 0$, and is an even smaller fraction of that at large ν . By 10 kcal/mol the minimum has almost disappeared and the distinction between the tight and roaming mechanisms is blurred.

III.B. CN_2 . Triplet CN_2 has three stable isomers, linear NCN and CNN , and a higher energy, shallow, C_{2v} ring species. Moskaleva et al.³⁸ have shown that the two linear isomers can isomerize via a pathway involving the ring species and two tight, ring-opening/closing, saddle points. They also note that there is no barrier for the addition of N and CN to form either of the linear isomers. This suggests that there should be a roaming type isomerization pathway in which the molecule nearly fragments to $\text{N} + \text{CN}$, the nitrogen atom orbits around the CN fragment and finally reattaches to the other end of the CN fragment. In this particular case the roaming pathway is not expected to be important because the $\text{N} + \text{CN}$ asymptote lies ~ 35 kcal/mol above the barrier for the tight isomerization. However, this is still a useful example to study the connectivity and separability of the tight and roaming pathways. For our purposes we will ignore the existence of the shallow ring minimum and the lower ring-opening saddle point (to NCN) and examine the connectivity between the roaming saddle point and the higher ring-opening saddle point (to CNN).

The geometries, frequencies, and energies of the relevant stationary points are summarized in Table 2, and a plot of the potential surface is given in Figure 7. Figure 7 is qualitatively quite similar to Figure 3, showing two first-order saddle points separated by a second-order saddle point. In this case, however, the second-order saddle point is much higher and broader than in MgH_2 . The CNN angle varies by over 20° (compared to less than 2° for MgH_2) for the three saddle points, implying a more highly curved ridge separating reactants and products. Nonetheless, we can still attempt to follow the ridge using the SPP algorithm outlined above for MgH_2 . If we take as our distinguished coordinate the distance from the midpoint of the CN bond to the second nitrogen atom, we obtain the SPP shown in Figure 8. Again we find this SPP passes very close to all three saddle points implying we have a reasonable representation of the ridge.

Table 2. (10E,9O)-CASPT2/cc-pVTZ Geometries, Frequencies, and Energies of the Stationary Points on the CN₂ Potential Surface

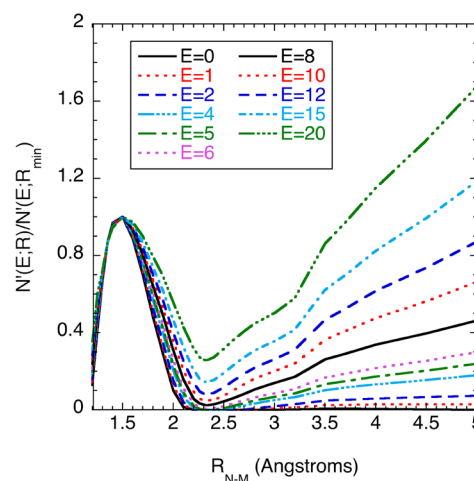
	NCN	N + CN	CNN	tight SP	roaming SP	2nd-order SP
R_{CN} (Å)	1.237	1.180	1.239	1.237	1.180	1.189
R_{NN} (Å)			1.212	1.470	3.449	2.290
$\angle\text{C-N-N}$ (deg)	180.0		180.0	72.9	95.6	87.8
ω_1 (cm ⁻¹)	1651	2045	1473	1753	2037	1897
ω_2 (cm ⁻¹)	1230		1230	727	40	558i
ω_3 (cm ⁻¹)	881(×2)		434(×2)	557i	23i	296i
energy (kcal/mol)	-105.9	0.0	-76.4	-30.9	-0.3	5.4

**Figure 7.** Contour plot for the interaction of an N atom with a rigid CN radical. The contour interval for the thick (thin) contours is 5.0 (0.1) kcal/mol. Other plotting conventions are as in Figure 3.**Figure 8.** SPP for the isomerization of CN₂ as a function of the distance between one nitrogen atom and the midpoint of the remaining CN fragment. The solid red dots correspond to the first- and second-order saddle points.

The plot in Figure 8 indicates an energetic separability of the tight and roaming mechanisms for energies up to 5 kcal/mol relative to CN + N. The dynamic separability was also explored via a determination of the differential contribution N' as a function of the separation $R_{\text{N-M}}$. For this case, we evaluated the CN stretching frequency and overall rotational constants along

the SPP and then used rigid rotor harmonic oscillator assumptions to evaluate the number of states.

The calculated N' values are illustrated in Figure 9 for a range of excess energies relative to CN + N. The mechanism divider

**Figure 9.** Plot of the normalized differential contribution to the transition state number of states $N'(R_{\text{N-M}})$ as a function of the separation $R_{\text{N-M}}$ between the N atom and the midpoint of CN. The normalization is relative to the value at the minimum in the potential on the global dividing surface ($R_{\text{N-M}} = 1.4$ Å; cf. Figure 8). The different lines denote N' values for different energies in kcal/mol relative to CN + N.

surfaces (i.e., the minima in the differential contributions) again correlate with the second-order saddle point. Notably, in this case the dynamic separability persists to high energy and the presumption of distinct tight and roaming isomerization mechanisms is widely appropriate. Even at an excess energy of 20 kcal/mol the contribution at the second-order saddle point is only 30% of that at the minimum in the potential for the global transition state dividing surface. Note that anharmonic vibrational effects will have little bearing on these plots because the only vibrational mode for the N' evaluations is of high frequency (~ 1900 cm⁻¹) throughout.

IV. FORMALDEHYDE AND ACETALDEHYDE

Far more has been written about roaming radical mechanisms in formaldehyde and acetaldehyde than for any other cases. Nonetheless, questions as to the separability of the roaming and tight pathways for both these systems continue to be raised.^{39,40} Unfortunately, the high dimensionality of these systems has, to date, made it impossible to follow the ridges connecting the tight and roaming saddle points.

IV.A. Formaldehyde. The first reported attempt to characterize an approximate ridge for formaldehyde was by

Bowman et al.³⁹ who simply linearly interpolated in internal coordinates between the two saddle points (cf. our Model 2). The path one obtains from this approach depends on the choice of internal coordinates used in the interpolation. In Figure 10 we show linear interpolations in two different

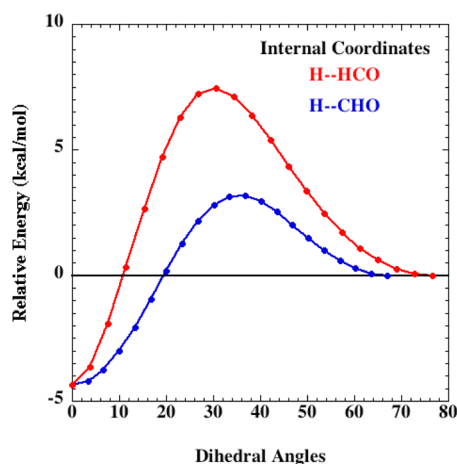


Figure 10. Potential energy curves resulting from linearly interpolating between the geometries of the tight and roaming saddle points for formaldehyde. The internal coordinates used for the blue curve include the CO distance, two CH distances and two HCO angles. The internal coordinates for the red curve replaces one of the CH distances with the HH distance and one of the HCO angles with the HHC angle.

coordinate systems, one giving a barrier of ~ 3 kcal/mol (in agreement with Bowman et al.) and the other giving a barrier of ~ 8 kcal/mol. Our attempts to locate a second-order saddle point near these maxima failed, implying neither path is a good approximation to the ridge that contains the second-order saddle point; i.e., the ridge must be highly curved in these coordinates. As discussed in section II and the Appendix, one would not expect such an interpolation to be a useful choice of global dividing surface, as the dividing surface connecting these two saddle points should be locally perpendicular to their reaction coordinates. Such a simple interpolation worked well for the triatomic examples discussed above because for those systems the two reaction coordinates were similar. This is not the case for formaldehyde. The character of the reaction coordinate for the tight saddle point is primarily an in-plane bending of the hydrogen closest to the CO, whereas the reaction coordinate for the roaming saddle point is an almost entirely out-of-plane, orbiting (torsional) motion of the roaming hydrogen atom.

Subsequently, Shepler et al.⁴⁰ reported a two-dimensional scan of the potential energy surface between the two saddle points, again linearly interpolating the internal coordinates between the two structures. Using this approach they found a path having no barrier connecting the two saddle points. In Figure 11 we show the results of a similar calculation. The barrierless path Shepler et al. describe begins at the roaming saddle point (marked with the letter R in Figure 11) descends vertically along the dihedral angle coordinate and eventually curves to the left to connect with the tight saddle point (marked with the letter T). As discussed in section II, this path is problematic because near the roaming saddle point it involves motion along the roaming reaction coordinate (which as noted above is almost entirely torsional motion). *In fact, any path that*

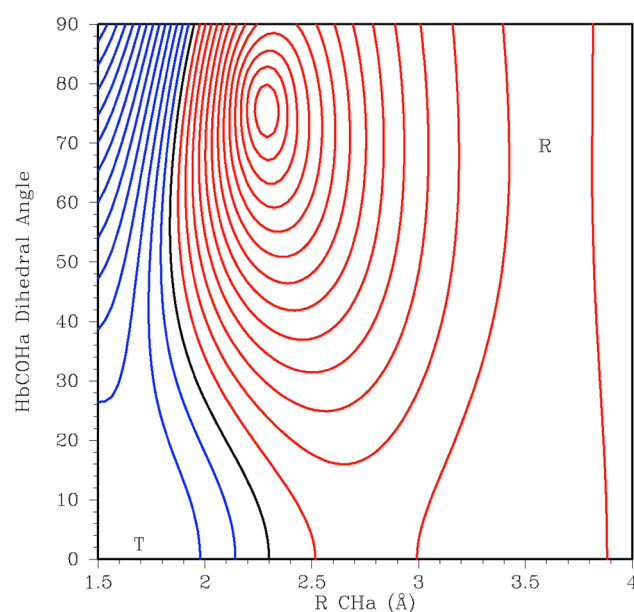


Figure 11. Formaldehyde potential energy surface resulting from the two-dimensional linear interpolation of the geometries of the tight and roaming saddle points. R indicates the location of the roaming saddle point. T indicates the location of the tight saddle point.

decreases in energy as it moves away from the first-order saddle point necessarily has a high overlap with the reaction coordinate.

A better approximation to the ridge can be obtained by initially moving away from the roaming saddle point in the horizontal direction of Figure 11, which is the CH stretching coordinate and has little overlap with the roaming reaction coordinate. This takes us toward what looks like a second-order saddle point at a CH distance of ~ 2.25 Å and a dihedral angle of $\sim 75^\circ$ in the interpolated potential energy surface of Figure 11. When a search for a second-order saddle point was initiated from this point, the calculation converged to the minimum energy point on a conical intersection previously reported by Araujo et al.⁴¹ Note that a minimum energy point on a conical intersection is similar to a second-order saddle point, where, instead of two imaginary frequencies, the conical intersection may be characterized as having two coordinates that break the degeneracy of the intersecting states.⁴² The lower-energy state therefore behaves like a second-order saddle point near the conical intersection, except that a two-dimensional cusp (having two “infinite” imaginary frequencies) is formed instead of a second-order saddle point. The two coordinates defining the cusp may be used analogously with the two imaginary frequencies of a second-order saddle point to define the orientation of the dividing surface. It appears then that, for formaldehyde, the conical intersection acts as the barrier on the ridge separating the two first-order saddle points. This conical intersection has an energy of 11 kcal/mol relative to the H + HCO asymptote.

To improve upon Model 2, we may define our global dividing surface to pass through the conical intersection, as in Model 3. We confirmed the connectivity of the conical intersection and the two first-order saddle points by following linearly interpolated paths from the conical intersection to each of the first first-order saddle points. Furthermore, we do this for both choices of internal coordinate systems used in Figure 10. The resulting approximate ridge profiles are displayed in Figure 12, plotted as a function of the HCO angle that both coordinate

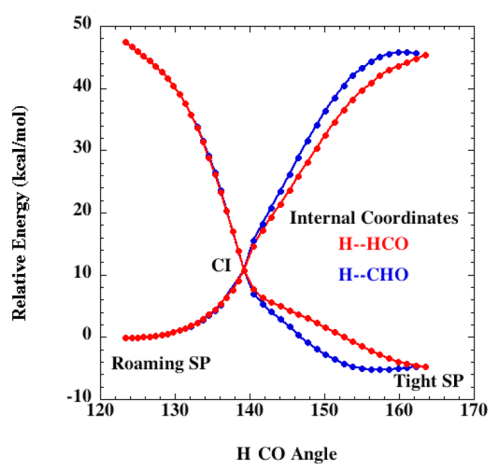


Figure 12. Potential energy curves resulting from linearly interpolating between the geometries of the tight saddle point, the conical intersection, and the roaming saddle point for formaldehyde. The internal coordinates are as defined in Figure 10.

systems have in common. From this plot it can be seen that the energy varies nearly monotonically from the conical intersection down to both first-order saddle points independent of the choice of internal coordinates.

The plot in Figure 12 indicates an energetic separability of the tight and roaming mechanisms up to 11 kcal/mol. We have not explored the dynamic separability for formaldehyde because the change from a second-order saddle point to a conical intersection complicates the analysis. Nevertheless, the results for the MgH_2 and CN_2 cases clearly suggest that the tight and roaming mechanisms will remain dynamically distinct to excess energies of 20 kcal/mol or more. This conclusion is consistent with the experimental results, which show two distinct product populations.¹

IV.B. Acetaldehyde. Shepler et al.⁴⁰ have also reported a linearly interpolated path connecting the tight and roaming saddle points in acetaldehyde, finding a barrier of 6 kcal/mol. In Figure 13 we show two such linearly interpolated paths, again for two different choices of internal coordinates. Again the resulting energy profiles are very different. For the case when one of the internal coordinates is the distance between the

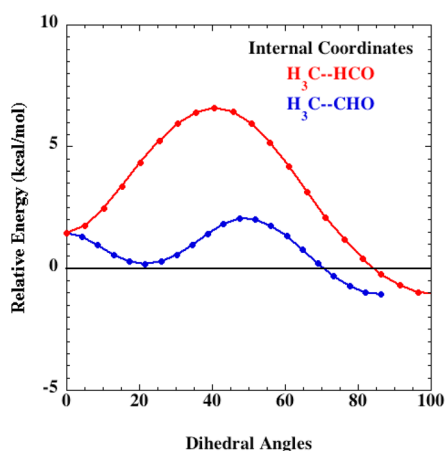


Figure 13. Potential energy curves resulting from linearly interpolating between the geometries of the tight and roaming saddle points for acetaldehyde.

methyl carbon and the HCO hydrogen, we obtain a curve (shown in red in Figure 13) similar to that reported by Shepler et al. However, for the case where this distance coordinate is replaced by the CC distance, we find a dramatically different profile, shown in blue in Figure 13. The blue profile exhibits multiple minima and has almost no net barrier separating the two saddle points. For the reasons discussed above, neither of these linearly interpolated paths is expected to be a good approximation to the ridge.

Starting a search at a geometry analogous to that of the conical intersection in formaldehyde we find a similar conical intersection for acetaldehyde. To our knowledge this conical intersection has not been previously reported. The structure of the conical intersection is shown in Figure 14. Again, as a check

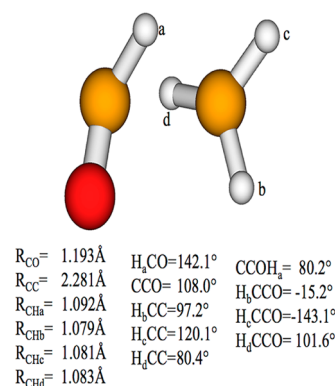


Figure 14. Structure of the conical intersection in acetaldehyde from multistate CASPT2 calculations.

on the connectivity of the first-order saddle points and the conical intersection, we follow linearly interpolated paths from the conical intersection to each of the saddle points. The results, shown in Figure 15, suggest that this conical intersection is the barrier on the ridge connecting the two first-order saddle points (as was found for formaldehyde). This barrier is predicted to be ~ 12 kcal/mol above the $\text{CH}_3 + \text{HCO}$ asymptote.

The plot in Figure 15 indicates an energetic separability of the tight and roaming mechanisms up to an excess energy of 12

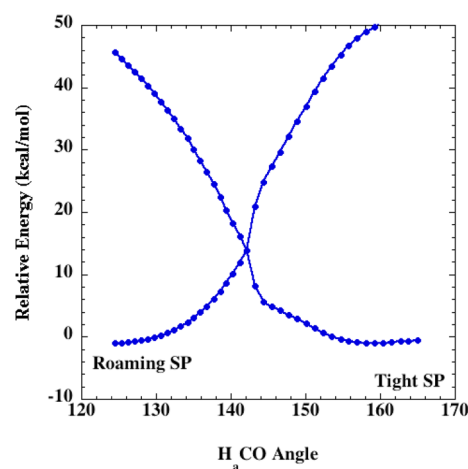


Figure 15. Potential energy curves resulting from linearly interpolating between the geometries of the tight saddle point, the conical intersection, and the roaming saddle point for acetaldehyde.

kcal/mol, and they are likely dynamically distinct to much higher energies.

V. HNNOH

The decomposition of HNNOH is a key step in the thermal de- NO_x process.⁴³ HNNOH is formed via the addition of NH_2 and NO making NH_2NO , which then isomerizes to HNNOH. HNNOH can decompose via a tight saddle point to $\text{N}_2 + \text{H}_2\text{O}$ or via simple bond cleavage to make the radicals, $\text{HNN} + \text{OH}$.⁴⁴ In Figure 16 we show a plot adapted from ref 44,

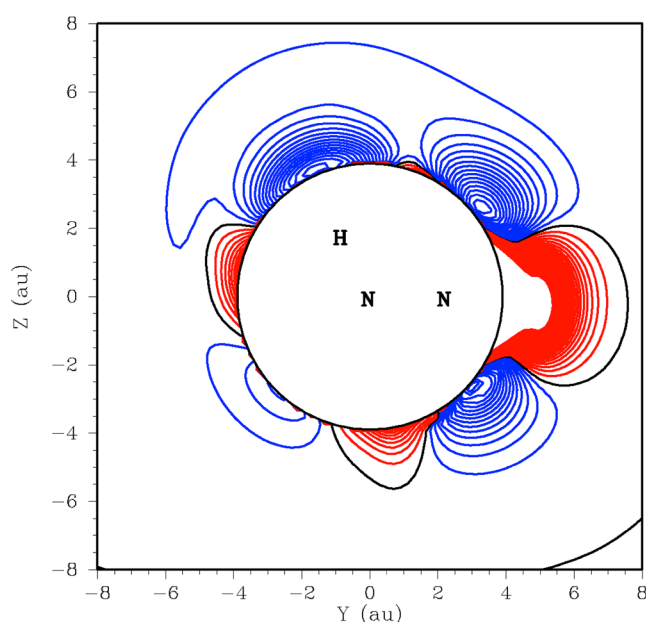


Figure 16. Contour plot for the interaction of a rigid OH radical with a rigid NNH radical. The contour interval is 2 kcal/mol. Both the HON angle and the HONN dihedral angle are fixed at 90° . Other plotting conventions are as in Figure 3. Adapted from ref 44.

showing the NHH + OH interaction potential. In this plot the cis and trans HNNOH species can be seen as the two attractive regions on the right and the $\text{OH} + \text{HNN} \rightarrow \text{H}_2\text{O} + \text{N}_2$ disproportionation path can be seen in the upper left. There also is what appears to be a roaming type saddle point with (Y, Z) coordinates of $(\sim 1, \sim 5)$ that connects the cis radical dissociation path to the disproportionation path. However, all attempts to find a true saddle point in this region failed with the optimizations collapsing to the much lower energy tight saddle point for molecular elimination, $\text{HNNOH} \rightarrow \text{H}_2\text{O} + \text{N}_2$. To better understand the connection between the tight saddle point and the roaming region of the potential surface shown in Figure 16, we evaluate a SPP using the NO distance as the distinguished coordinate. The result is shown in Figure 17 where it is compared to a harmonic treatment for the NO stretch coordinate of the tight saddle point.

The plot in Figure 17 would seem to suggest that there is no distinction between the tight and roaming mechanisms for HNNOH. Nevertheless, we have again evaluated the differential contributions N' for a few selected NO separations R_{NO} . We assume rigid rotor harmonic oscillator energies for the motions orthogonal to the assumed SPP coordinate R_{NO} . Though these assumptions will not be quantitatively correct, especially in the “roaming” region, they should provide at least

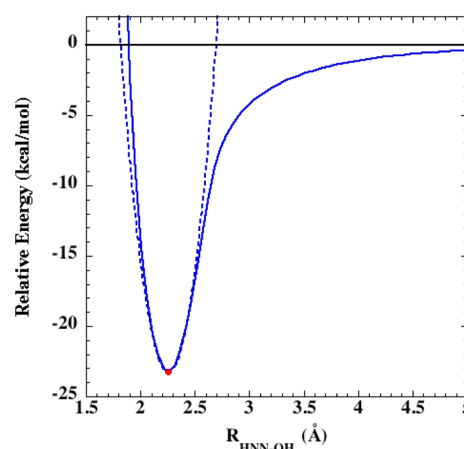


Figure 17. Potential curves for the dissociation of HNNOH as a function of the NO distance. The solid line is the SPP as described in the text. The dashed line is a harmonic approximation to the saddle point, NO stretch. The red dot corresponds to the tight saddle point for the reaction $\text{HNNOH} \rightarrow \text{H}_2\text{O} + \text{N}_2$. The energies are relative to the $\text{NNH} + \text{OH}$ asymptote.

a semiquantitatively correct description of the variation in N' along the SPP.

The calculated differential contributions are illustrated in Figure 18 for a range of excess energies relative to $\text{HNN} + \text{OH}$.

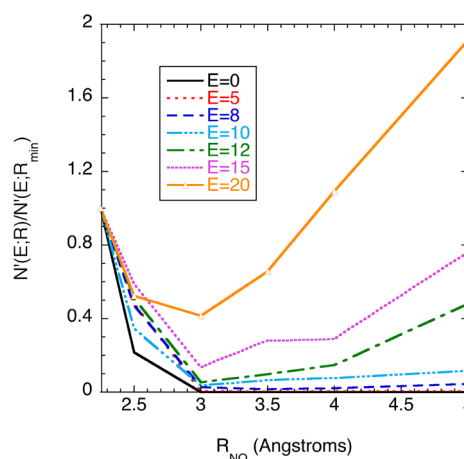


Figure 18. Plot of the normalized differential contribution to the transition state number of states N' as a function of the separation R_{NO} between the O atom and the central N atom. The normalization is relative to the value at the minimum in the potential on the global dividing surface ($R_{\text{NM}} = 2.25$ Å; cf. Figure 17). N' values for various energies E in kcal/mol relative to $\text{HNN} + \text{OH}$ are shown.

Notably, each of the lines shows a minimum at a NO separation of 3 Å, indicating the clear existence of a mechanism divider surface. Furthermore, this minimum is quite pronounced. For example, for an excess energy of 15 kcal/mol, the minimum is just $\sim 15\%$ of both the value at the potential minimum for the global dividing surface and the value at large R_{NO} . Thus, even in this case, where there is neither a roaming saddle point nor a second-order saddle point, there is some dynamic separation into tight and roaming mechanisms. The plot also indicates that the roaming contribution to the number of states at the transition state likely becomes significant already by about 10 kcal/mol. For energies in this range or higher, simple rigid rotor harmonic oscillator estimates based on the tight transition state

will clearly be inadequate. We note that an excess energy of 10 kcal/mol corresponds to an effective temperature of 600 K for a system of eight classical harmonic oscillators. Thus, an accurate prediction of the branching in $\text{NH}_2 + \text{NO}$ at combustion temperatures must include a treatment of both the tight and roaming contributions.

VI. CONCLUSIONS

The second-order saddle point on the ridge containing the two first-order saddle points provides a useful measure of the energetic separability of the two related saddle points. Energetic separability guarantees dynamic separability, but the converse is not true. Simple global dividing surfaces can be constructed from information about only the first-order saddle points (Models 1 and 2). Information about the second-order saddle points allows for systematic and substantial improvements of these dividing surfaces (Model 3), with information about the SPP's yielding further improvements. Simple variational optimizations should yield meaningful global dividing surfaces that are also locally optimal. In this context, conical intersections can be viewed as generalized second-order saddle points, and they play the same role in the development of global dividing surfaces for some systems.

Evaluations of the differential contributions to the reactive flux along approximate SPP's provide indications of the dynamic separability of the roaming and tight mechanisms. The location of the $n-2$ -dimensional surface where the differential contribution is minimized provides an approximate separation between the mechanisms. We label this surface the mechanism divider surface. The smaller the flux at the mechanism divider is relative to the maximum in the flux near the first-order saddle points, the greater is the separability of the mechanisms. The mechanism divider surface is often, but not always, associated with a second-order saddle point or conical intersection connecting the two first-order saddle points along the SPP.

There is a wide variability in the degree to which roaming and tight saddle point mechanisms connecting the same reactants and products are energetically separable. Remarkably, even for the $\text{HNN} + \text{OH}$ reaction, where there is no energetic separability, the roaming and tight mechanisms are dynamically separable to quite a high energy. The finding of a strong dynamic separability up to quite high energy for all examples studied here is likely a fairly general result.

■ APPENDIX

A.1. Electronic Structure Methods

Because the focus of this paper is qualitative in nature, the details of the electronic structure methods are not particularly important. However, for completeness we briefly summarize here the levels of electronic structure theory used in each of the examples discussed above. All electronic structure calculations were carried out with the Molpro program package.⁴⁵

HCO_2 : The results shown in Figure 1 were obtained using internally-contracted, multireference configuration interaction calculations (MRCI).^{46,47} The calculations employed a 7 orbital (6 CO_2 π orbitals plus the hydrogen 1s orbital), 9 electron active space and the Dunning aug-cc-pVDZ basis set.⁴⁸ The CASSCF calculations were state averaged over two states with dynamical weighting. Only the OH distance (R) and the HOCO dihedral angle were varied. The remaining geometrical parameters were kept fixed at the values for the cis saddle point.

MgH_2 : The results shown for MgH_2 were also obtained using internally-contracted, MRCI.^{46,47} The calculations employed a full valence active space (4 electrons in 6 orbitals) and the Dunning cc-pVQZ basis set.^{49,50}

CNN: The results shown for the isomerization of CNN were obtained using second-order, multireference, perturbation theory (CASPT2).⁵¹ The calculations employed an active space consisting of 10 electrons in 9 orbitals (all of the valence p orbitals) and the Dunning cc-pVTZ basis set.⁴⁹

H_2CO : The formaldehyde results were obtained using CASPT2, with a 9 orbital and 10 electron active space and the Dunning aug-cc-pVTZ basis set.⁴⁸ For the calculations in the vicinity of the conical intersection, the CASSCF calculations were state averaged over the two states involved in the crossing and we used the multistate variant of CASPT2.⁵²

CH_3CHO : The acetaldehyde results were obtained using CASPT2, with a 3 orbital and 2 electron active space and the Dunning aug-cc-pVTZ basis set.⁴⁸ Again, for the calculations in the vicinity of the conical intersection, the CASSCF calculations were state averaged over the two states involved in the crossing and we used the multistate variant of CASPT2.

HNNOH: The results shown in Figure 16 for HNNOH are derived from CASPT2 calculations with a 7 orbital and 8 electron active space and the Dunning aug-cc-pVDZ basis set.⁴⁸ The CASSCF calculations were state-averaged over the two components of the OH, $^2\Pi$ fragment.

A.2. Mathematical Formulation of Model Global Dividing Surfaces and Separability of State Counts

1. Defining the Geometry of the Transition State Dividing Surface. In nonvariational TST one typically defines the dividing surface as passing through a first-order saddle point, perpendicular to the normal mode vector, $\hat{\mathbf{x}}^{(0)}$, associated with the imaginary frequency. (The notation $\hat{\mathbf{a}}$ denotes a unit vector in the direction of \mathbf{a} .) Such a planar dividing surface is defined by the constraint

$$\mathbf{Q} \cdot \hat{\mathbf{x}}^{(0)} = 0 \quad (\text{A1})$$

where the n internal nuclear coordinates are labeled \mathbf{Q} . The resulting $n-1$ -dimensional collection of geometries that satisfies eq A1 is labeled q . Although this "conventional" TST prescription is generally useful, there are also many instances where this prescription is not accurate, as the optimal dividing surface moves away from the saddle point or changes orientation.

A useful series of candidate dividing surfaces for variational transition state minimizations can be obtained by following the intrinsic reaction coordinate (IRC) downhill from the saddle point. Coordinates along this path may be labeled by the reaction coordinate s , which describes the mass-scaled distance along the IRC from the saddle point toward either the reactants (negative s) or the products (positive s). Alternatively, in some cases it is simpler, and reasonably appropriate, to consider the analogous variations along a distinguished coordinate minimum energy path (MEP). Along the IRC (or MEP) but displaced from the saddle point, one can define useful dividing surfaces as perpendicular to the nuclear gradient, and we label the unit vector in this direction $\hat{\mathbf{x}}^{(s)}$. Equation A1 is generalized to

$$\mathbf{Q} \cdot \hat{\mathbf{x}}^{(s)} = s \quad (\text{A2})$$

which describes a dividing surface perpendicular to $\hat{\mathbf{x}}^{(s)}$ and having the value s along the excluded coordinate. We note that

one may also variationally optimize $\hat{\mathbf{x}}^{(s)}$ to point in directions other than the gradient.

The dividing surfaces discussed so far are all hyperplanes. One can relax this restriction by introducing additional geometric parameters and writing

$$\mathbf{Q} \cdot \hat{\mathbf{x}}^{(s)}(\mathbf{Q}) = s \quad (\text{A3})$$

where now $\hat{\mathbf{x}}^{(s)}$ can point in different directions at different parts of the dividing surface. Of course, care must be taken to ensure that the resulting dividing surface is continuous. In the local vicinity of the IRC, one may expect $\hat{\mathbf{x}}^{(s)}(\mathbf{Q})$ to variationally optimize to $\hat{\mathbf{x}}^{(s)}$. If there is significant flux away from the reaction path, the additional flexibility in eq A3 may allow for more accurate predictions than those obtained with eq A2.

Finally, we note that dividing surfaces need not be defined relative to saddle points or IRCs or MEPs. For example, when describing barrierless reactions, one may obtain useful dividing surfaces by constraining the center-of-mass separations of the reactants or using generalized dividing surfaces based on constraining the distance between pivot points displaced from the centers of mass. The index s may be generalized and associated with the pivot point distances.

In summary, dividing surfaces may be defined by their normal $\hat{\mathbf{x}}^{(s)}$ and by the value along this excluded coordinate s . Most generally, $\hat{\mathbf{x}}^{(s)}$ can be a function of geometry, as in $\hat{\mathbf{x}}^{(s)}$, subject to the constraints that the dividing surface is continuous and completely separates reactants from products.

2. Counting States on the Dividing Surface. A standard expression for the classical state count for an arbitrary dividing surface was provided in eq 3 of the text. In principle, this state count can be evaluated exactly for a given potential energy surface and dividing surface, although it is difficult to do so in practice. Instead, one typically makes additional assumptions when evaluating $N_E^{(s)}$, and one often wishes to use quantum mechanical formulas instead of classical ones. One choice is to use quantum mechanical RRHO state counts, along with rotational constants and harmonic vibrational frequencies obtained from the saddle point geometry for $s = 0$ and evaluated along the reaction path for $s \neq 0$. This quantum mechanical RRHO TST prescription can be accurate, but there are many applications where its accuracy can be questioned. When the harmonic frequencies are very small, for example, the harmonic oscillator approximation is not expected to be accurate.

Whatever the level of theory used to approximate $N_E^{(s)}$, the state counts may then be variationally optimized with respect to $\hat{\mathbf{x}}^{(s)}$ (or $\hat{\mathbf{x}}^{(s)}$) and s for each total energy to obtain estimates for N_E^\ddagger from which variational TST rate coefficients are obtained.

3. Sparability of Multiple Reaction Paths. As discussed in section II, there is necessarily a single $n-1$ -dimensional dividing surface that completely separates reactants from products for any reaction where a rate can be meaningfully defined, even reactions with multiple pathways leading from the same reactants to the same products. It can nonetheless be practically convenient to represent such a global dividing surface in terms of its contributions from different reaction pathways. In addition to facilitating the calculation, such a separation provides a useful conceptual picture for physically interpreting the relative importance of competing reaction mechanisms.

Such a separation is especially relevant for the molecular decomposition reactions considered here, which feature both tight and roaming saddle points. For clarity we limit the present

discussion to systems with two saddle points connecting the same set of reactants and products.

For the dissociation of HOCO discussed in section II, the imaginary-frequency normal mode vectors for the cis (C) and trans (T) saddle points are similar ($\hat{\mathbf{x}}_C = \hat{\mathbf{x}}_T \approx \hat{\mathbf{R}}$, where $\hat{\mathbf{R}}$ is a unit vector in the direction of the radial coordinate R), but the values of R at the two saddle points (R_C and R_T) are not. The global dividing surfaces discussed qualitatively in section II and shown in Figure 1 are presented in more detail here. The surfaces are interpolated as a function of a single coordinate ϕ such that they may be defined

$$R = c_C(\phi)R_C + c_T(\phi)R_T \quad (\text{A4})$$

The two blue lines in Figure 1 correspond to either $c_C = 1$ and $c_T = 0$ or $c_T = 1$ and $c_C = 0$. An improved global surface was suggested to pass through *both* saddle points, i.e.,

$$c_C(\phi_C) = 1 \quad (\text{A5a})$$

$$c_T(\phi_T) = 1 \quad (\text{A5b})$$

For simple linear interpolations satisfying eq A5, the resulting global dividing surface will *not* satisfy

$$\hat{\mathbf{x}}^{(s)}(\mathbf{Q}) = \hat{\mathbf{x}}_A^{(s)} \quad \text{for } \mathbf{Q} \text{ near } \mathbf{Q}_A \quad (\text{A6})$$

where $A = C$ and T ; i.e., the resulting global dividing surface will not be locally orthogonal to the reaction coordinate at each saddle point. Specifically, if we define (one segment of) the linearly interpolated global surface as

$$f(\mathbf{Q}) = \frac{R - R_T}{R_C - R_T} - \frac{\phi - \phi_T}{\phi_C - \phi_T} = 0 \quad \text{for } \phi_C > \phi > \phi_T \quad (\text{A7})$$

we can calculate its normal by taking the gradient of eq A7, i.e.,

$$\begin{aligned} x_R &= \nabla f \cdot \hat{\mathbf{R}} = \frac{1}{R_C - R_T} \\ x_\phi &= \nabla f \cdot \hat{\phi} = \frac{-1}{\phi_C - \phi_T} \\ x_\alpha &= 0 \end{aligned} \quad (\text{A8})$$

where α is any coordinate other than R and $\hat{\phi}$ and $\hat{\mathbf{x}}_i$ are the components of $\hat{\mathbf{x}} = \mathbf{x}/|\mathbf{x}|$. The normal defined by eq A8 is clearly not in the direction of the reaction coordinate $\hat{\mathbf{R}}$. If instead one interpolates the dividing surface as

$$\begin{aligned} f(\mathbf{Q}) &= R - R_T \sin^2 \frac{\phi}{2} - R_C \cos^2 \frac{\phi}{2} = 0 \\ \text{for } \phi_C &> \phi > \phi_T \end{aligned} \quad (\text{A7'})$$

then

$$\begin{aligned} x_R &= \nabla f \cdot \hat{\mathbf{R}} = 1 \\ x_\phi &= \nabla f \cdot \hat{\phi} = 2(R_C - R_T) \sin \frac{\phi}{2} \cos \frac{\phi}{2} \\ x_\alpha &= 0 \end{aligned} \quad (\text{A8'})$$

which is in the direction of $\hat{\mathbf{R}}$ for $\phi = \phi_C(0^\circ)$ and $\phi_T(180^\circ)$ as desired. The above procedure can be generalized to create global dividing surfaces that pass through multiple first- and second-order saddle points and that are locally orthogonal to

the imaginary-frequency normal mode vectors at the first-order saddle points.

Next we consider a series of simple models designed to illustrate dynamic separability in transition state theory calculations for reactions with one roaming R and one tight T saddle point connecting the same sets of reactants and products. The models are organized by the amount of information required to construct them and by their complexity. The simplest models (Models 0 and 1) only require information about the first-order saddle points and do not involve interpolation. In Model 2, global dividing surfaces are obtained by interpolating between the two first-order saddle points. Model 3 requires additional information at the intermediate second-order saddle point. Model 4 employs generalized linear surfaces intersecting to create a global surface subject to variational optimizations. Finally, the SPP model requires the existence of an SPP that smoothly connects the second-order saddle point to both first-order saddle points.

Model 0. For completeness, we define Model 0 as the use of dividing surfaces appropriate for a single saddle point as global dividing surfaces. For example, one could calculate a total rate coefficient using dividing surfaces based on the saddle point associated with one conformer of a system with a torsion. With appropriate treatments of anharmonicity, such a model may be useful.

Model 1a. Model 1 is the simplest model that requires information about both saddle points. Here, the roaming and tight processes are assumed to be separable, i.e.,

$$N_E^\ddagger = N_{E,R}^\ddagger + N_{E,T}^\ddagger \quad (\text{A9})$$

Within this approximation, independent TST calculations can be carried out using dividing surfaces appropriate for each process, i.e.,

$$\mathbf{Q} \cdot \hat{\mathbf{x}}_R^{(s)} = s_R \quad (\text{A10a})$$

and

$$\mathbf{Q} \cdot \hat{\mathbf{x}}_T^{(s)} = s_T \quad (\text{A10b})$$

for $N_{E,R}^\ddagger$ and $N_{E,T}^\ddagger$, respectively. The set of geometries satisfying eqs A10a and A10b are labeled $q_R^{(s)}$ and $q_T^{(s)}$, respectively. The fundamental assumption of Model 1a is that these two sets do not overlap in energetically accessible regions of the potential energy surface.

Model 1b. In general, the dividing surfaces defined by eqs A10a and A10b will intersect one another in an $n-2$ -dimensional space, and we label the geometries in this space $q_2^{(s)}$. The intersection space $q_2^{(s)}$ defines two halves of each of the spaces $q_R^{(s)}$ and $q_T^{(s)}$, and we denote the halves that contain the associated saddle points as $\bar{q}_R^{(s)}$ and $\bar{q}_T^{(s)}$, respectively. Model 1b defines the space of the transition state dividing surface q to be the union of $\bar{q}_R^{(s)}$ and $\bar{q}_T^{(s)}$. This dividing surface satisfies eq A6, is continuous (unlike Model 1a), and fully separates reactants and products. Model 1b defines a global dividing surface as the union of segments associated with each transition state, which aids in the discussion of separability as the flux through $\bar{q}_R^{(s)}$ and $\bar{q}_T^{(s)}$ can be unambiguously associated with SP_R and SP_T , respectively, and identifies the intersection space $q_2^{(s)}$ as defining the critical surface separating the two segments.

(For some cases the surfaces do not intersect, as illustrated for HCO_2 in Figure 1. When this is the case, one could define curved surfaces that intersect. Alternatively, one could define a

third surface that intersects and joins the two. This model will be generalized as Model 4 below.)

To characterize the separability of the roaming and tight processes, it is useful to identify the minimum-energy geometry in the intersecting space of $q_2^{(s)}$ as $\mathbf{Q}_2^{(s)}$ and its energy $E_2^{(s)}$. For $E < E_2^{(s)}$, Model 1a and 1b give identical predictions, and one may unambiguously say that the processes are separable for this choice of dividing surfaces. For $E > E_2^{(s)}$, the dividing surfaces sampled in Model 1a are not properly delimited, and Model 1a will in general overcount N_E^\ddagger due to this error. The energy of $E_2^{(s)}$ relative to E therefore provides one criterion for discussing separability. As discussed in section III though, *dynamic* separability is more relevant to mechanistic ideas of separability, and it may hold even when *energetic* separability does not.

Model 2a. In Model 2, we define a dividing surface by using the directions of the imaginary frequency normal mode vectors at the roaming and tight saddle points to interpolate between the roaming and tight saddle points. Using linear interpolations (Model 2a), such a dividing surface is defined piecewise by

$$f(\mathbf{Q}) = \frac{\mathbf{Q} \cdot \hat{\mathbf{x}}_T^{(s)} - \mathbf{Q}_T \cdot \hat{\mathbf{x}}_T^{(s)}}{\mathbf{Q}_R \cdot \hat{\mathbf{x}}_T^{(s)} - \mathbf{Q}_T \cdot \hat{\mathbf{x}}_T^{(s)}} - \frac{\mathbf{Q} \cdot \hat{\mathbf{x}}_R^{(s)} - \mathbf{Q}_T \cdot \hat{\mathbf{x}}_R^{(s)}}{\mathbf{Q}_R \cdot \hat{\mathbf{x}}_R^{(s)} - \mathbf{Q}_T \cdot \hat{\mathbf{x}}_R^{(s)}} = 0$$

for $\mathbf{Q}_T \cdot \hat{\mathbf{x}}_T^{(s)} < \mathbf{Q} \cdot \hat{\mathbf{x}}_T^{(s)} < \mathbf{Q}_R \cdot \hat{\mathbf{x}}_T^{(s)}$ (A11)

with similar equations for the other segments, where \mathbf{Q}_T and \mathbf{Q}_R are the geometries of the tight and roaming saddle points, respectively. The normal of this dividing surface is

$$x'_R = \nabla f \cdot \hat{\mathbf{x}}_R^{(s)} = \frac{-1}{\mathbf{Q}_R \cdot \hat{\mathbf{x}}_R^{(s)} - \mathbf{Q}_T \cdot \hat{\mathbf{x}}_R^{(s)}}$$

$$x'_T = \nabla f \cdot \hat{\mathbf{x}}_T^{(s)} = \frac{1}{\mathbf{Q}_R \cdot \hat{\mathbf{x}}_T^{(s)} - \mathbf{Q}_T \cdot \hat{\mathbf{x}}_T^{(s)}} \quad (\text{A12})$$

$$x'_\alpha = 0$$

which is not in the direction of the reaction coordinate at either saddle point.

Model 2b. As discussed above for HOCO, one could choose nonlinear interpolation schemes that are functions of the interpolation coordinates designed to satisfy

$$\hat{\mathbf{x}}'_R = \nabla f \cdot \hat{\mathbf{x}}_R^{(s)} = 1$$

$$x'_T = \nabla f \cdot \hat{\mathbf{x}}_T^{(s)} = 0$$

$$x'_\alpha = 0 \quad (\text{A13a})$$

for $\mathbf{Q} = \mathbf{Q}_R$ and

$$\hat{\mathbf{x}}'_R = \nabla f \cdot \hat{\mathbf{x}}_R^{(s)} = 0$$

$$\hat{\mathbf{x}}'_T = \nabla f \cdot \hat{\mathbf{x}}_T^{(s)} = 1$$

$$\hat{\mathbf{x}}'_\alpha = 0 \quad (\text{A13b})$$

for $\mathbf{Q} = \mathbf{Q}_T$, but these are not pursued in detail here. Instead, we simply note that linear interpolations cannot, in general, satisfy the requirement that the global dividing surface be locally orthogonal to the reaction coordinates at each of the saddle points. Model 2b is defined to be the use of some nonlinear interpolation scheme that enforces eqs A13. One can use the variational principle to numerically discriminate between competing interpolation schemes that satisfy eqs A13.

Model 3a. The linear interpolation schemes of Model 2a can be generalized to include the second-order saddle point, such that the global dividing surface consists of the segments connecting the first- and second-order saddle points. To motivate Model 3a, we note that this model defines the global dividing surface as a union of spaces associated with each saddle point, intersecting in a reduced dimensional space $q_2^{(s)}$. The space $q_2^{(s)}$ naturally delimits the contributions to the total flux from each of the two saddle points. If the definition of $q_2^{(s)}$ was not known but was given flexible geometric parameters, one could variationally improve the global dividing surface by maximizing the energy $E_2^{(s)}$ with respect to the two interpolation coordinates. If the optimization were sufficiently flexible, the resulting $q_2^{(s)}$ would include the second-order saddle point as its minimum energy geometry. The variational maximization of $E_2^{(s)}$ therefore motivates the inclusion of the second-order saddle point in the global dividing surface as well as its physical usefulness in separating the dynamical contributions associated with the two first-order saddle points.

Model 3b. For the same reasons discussed above for Model 2, the use of linear interpolations will not in general produce global dividing surfaces that are locally orthogonal to the reaction coordinates at each of the saddle points. One could again pursue nonlinear interpolation schemes, and these schemes define Model 3b.

Model 4a. Next we consider a model where the global dividing surface consists of three segments. We start with Model 1 and add a third linear dividing surface $q_A^{(s)}$ that intersects and joins the two. The global dividing surface is then the union of $q_R^{(s)}$, $q_T^{(s)}$, and $q_A^{(s)}$. Note that this scheme is less useful for studying separability as the flux through $q_A^{(s)}$ cannot be unambiguously assigned to R or T. Nonetheless, this scheme may be practically useful as it results in a realistic global dividing surface, avoids curved surfaces, is locally correct at the first-order saddle points, and does not require the location of the intermediate second-order saddle point. Variational optimizations could be used to guide the geometric specification of each of the segments. Because the surfaces are planar and two of them are defined as usual by the two first-order saddle points, practical implementations of variational optimizations using Model 4a could be made.

Model 4b. If one does know the second-order saddle point, one could guarantee that $q_A^{(s)}$ contains it, thus removing one parameter from the variational optimizations in Model 4a. Furthermore, it is reasonable that a variationally optimized $q_A^{(s)}$ will be perpendicular to some linear combination of the imaginary frequency normal modes for the second-order saddle point, and so one could define a model which contains only a single parameter (a mixing angle) defining the normal $q_A^{(s)}$ as some linear combination of the two imaginary frequency normal mode vectors at the second-order saddle point.

Model 4c. Finally, we note that it might be convenient to generalize Model 4b to consist of the union of more than three segments: $q_R^{(s)}$, $q_A^{(s)}$, $q_B^{(s)}$, ..., $q_T^{(s)}$. If each segment were subject to variational optimizations, it is reasonable to expect that each segment would essentially map to some segment of the SPP. In the limit of many segments, Model 4c converges to the SPP model, discussed next.

SPP Model. A series of constrained saddle point optimizations away from the proper saddle points for fixed values of the interpolation coordinates yields the most fundamental of the models discussed above. The resulting dividing surface is therefore perpendicular to at least one degree

of freedom along which the energy is maximized and follows a ridge connecting the two first-order saddle points to the second-order one. Again, dynamical considerations may shift the variationally preferred dividing surface away from this energetically derived one. Nonetheless, a SPP and the associated dividing surface provide a conceptually appealing means for carrying out TST calculations and for studying separability for reactions with multiple reaction paths.

These models suggest the usefulness of considering the potential energy surface as a function of the interpolation coordinates associated with the directions of the imaginary frequency normal mode vectors for the two first-order saddle points. Often, the character of these reaction coordinates can be associated closely with some internal coordinate (a stretch, bend, or torsion), which may be more convenient to use than the normal mode vectors. We considered such two-dimensional contour plots in the examples given in sections III–V.

AUTHOR INFORMATION

Notes

The authors declare no competing financial interest.

ACKNOWLEDGMENTS

This work was supported by the U.S. Department of Energy, Office of Basic Energy Sciences, Division of Chemical Sciences, Geosciences, and Biosciences, under Contract Numbers DE-AC02-06CH11357 (at ANL) and DE-AC04-94-AL85000 (at SNL).

REFERENCES

- (1) Townsend, D.; Lahankar, S. A.; Lee, S. K.; Chambreau, S. D.; Suits, A. G.; Zhang, S.; Rheinecker, J.; Harding, L. B.; Bowman, J. M. *Science* **2004**, 306, 1158–1161.
- (2) Suits, A. G. *Acc. Chem. Res.* **2008**, 41, 837–881.
- (3) Herath, N.; Suits, A. G. *J. Phys. Chem. Lett.* **2011**, 2, 642–647.
- (4) Van Zee, R. D.; Foltz, M. F.; Moore, C. B. *J. Chem. Phys.* **1993**, 99, 1664–1673.
- (5) Lahankar, S. A.; Chambreau, S. D.; Zhang, X.; Bowman, J. M.; Suits, F.; Suits, A. G. *J. Chem. Phys.* **2007**, 126, 044314-8.
- (6) Lahankar, S. A.; Goncharov, V.; Suits, F.; Farnum, J. D.; Bowman, J. M.; Suits, A. G. *Chem. Phys.* **2008**, 347, 288–299.
- (7) Houston, P. L.; Kable, S. H. *Proc. Natl. Acad. Sci.* **2006**, 103, 16079–16082.
- (8) Heazlewood, B. R.; Jordan, M. J. T.; Kable, S. H.; Selby, T. M.; Osborn, D. L.; Shepler, B. C.; Braams, B. J.; Bowman, J. M. *Proc. Natl. Acad. Sci.* **2008**, 105, 12719–12724.
- (9) Rubio-Lago, L.; Amaral, G. A.; Arregui, A.; Izquierdo, J. G.; Wang, F.; Zaouris, D.; Kitsopoulos, T. N.; Banares, L. *Phys. Chem. Chem. Phys.* **2007**, 9, 6123–6127.
- (10) Sivaramakrishnan, R.; Michael, J. V.; Klippenstein, S. J. *J. Phys. Chem. A* **2010**, 114, 755–764.
- (11) Harding, L. B.; Klippenstein, S. J.; Jasper, A. W. *Phys. Chem. Chem. Phys.* **2007**, 9, 4055–4070.
- (12) Klippenstein, S. J.; Georgievskii, Y.; Harding, L. B. *J. Phys. Chem. A* **2011**, 115, 14370–14381.
- (13) Audier, H. E.; Morton, T. H. *Org. Mass Spectrom.* **1993**, 28, 1218–1224.
- (14) Lee, J.; Grabowski, J. J. *Chem. Rev.* **1992**, 92, 1611–1647.
- (15) Marcy, T. P.; Diaz, R. R.; Heard, D.; Leone, S. R.; Harding, L. B.; Klippenstein, S. J. *J. Phys. Chem.* **2001**, 105, 8361–8369.
- (16) Klippenstein, S. J.; Miller, J. A.; Harding, L. B. *Proc. Combust. Inst.* **2002**, 29, 1209–1217.
- (17) Harding, L. B.; Georgievskii, Y.; Klippenstein, S. J. *J. Phys. Chem. A* **2010**, 114, 765–777.
- (18) Osborn, D. L. *Adv. Chem. Phys.* **2008**, 138, 213–265.
- (19) Pechukas, P. *Annu. Rev. Phys. Chem.* **1981**, 32, 59–77.

- (20) Fernandez-Ramos, A.; Miller, J. A.; Klippenstein, S. J.; Truhlar, D. G. *Chem. Rev.* **2006**, *106*, 4518–4584.
- (21) Baer, T.; Hase, W. L. *Unimolecular Reaction Dynamics: Theory and Experiments*; Oxford University Press: New York, 1996.
- (22) Gilbert, R. G.; Smith, S. C. *Theory of Unimolecular and Recombination Reactions*; Blackwell Scientific: Boston, 1990.
- (23) Wigner, E. *Trans. Faraday Soc.* **1938**, *34*, 29–41.
- (24) Keck, J. C. *J. Chem. Phys.* **1960**, *32*, 1035–1050.
- (25) Pechukas, P.; Pollak, E. *J. Chem. Phys.* **1979**, *71*, 2062–2068.
- (26) Miller, W. H. *Acc. Chem. Res.* **1976**, *9*, 306–312.
- (27) Miller, J. A.; Klippenstein, S. J. *J. Phys. Chem. A* **2003**, *107*, 2680–2692.
- (28) Miller, W. H. *J. Chem. Phys.* **1976**, *65*, 2216–2223.
- (29) Greenwald, E. E.; North, S. W.; Georgievskii, Y.; Klippenstein, S. J. *J. Phys. Chem. A* **2005**, *109*, 6031–6044.
- (30) Rehbein, J.; Carpenter, B. K. *Phys. Chem. Chem. Phys.* **2011**, *13*, 20906–20922.
- (31) Lourderaj, U.; Hase, W. L. *J. Phys. Chem.* **2009**, *113*, 2236–2253.
- (32) Pechukas, P.; McLafferty, F. J. *J. Chem. Phys.* **1973**, *58*, 1622–1625.
- (33) Maronsson, J. B.; Jonsson, H.; Vegge, T. *Phys. Chem. Chem. Phys.* **2012**, *14*, 2884–2891.
- (34) Zhou, D. D.; Han, K.; Zhang, P.; Harding, L. B.; Davis, M. J.; Skodje, R. T. *J. Phys. Chem. A* **2012**, *116*, 2089–2100.
- (35) Takayanagi, T.; Tanaka, T. *Chem. Phys. Lett.* **2011**, *504*, 130–135.
- (36) Li, H.; Xie, D.; Guo, H. *J. Chem. Phys.* **2004**, *121*, 4156–4163.
- (37) Klippenstein, S. J. *Chem. Phys. Lett.* **1993**, *214*, 418–424.
- (38) Moskaleva, L. V.; Lin, M. C. *J. Phys. Chem. A* **2001**, *105*, 4156–4163.
- (39) Bowman, J. M.; Shepler, B. C. *Annu. Rev. Phys. Chem.* **2011**, *62*, 531–553.
- (40) Shepler, B. C.; Han, Y.; Bowman, J. M. *J. Phys. Chem. Lett.* **2011**, *2*, 834–838.
- (41) Araujo, M.; Lasorne, B.; Bearpark, M. J.; Robb, M. A. *J. Phys. Chem. A* **2008**, *112*, 7489–7491.
- (42) Yarkony, D. R. *J. Chem. Phys.* **2001**, *114*, 2601–2613.
- (43) Miller, J. A.; Bowman, C. T. *Prog. Energy Combust. Sci.* **1981**, *15*, 287–338.
- (44) Fang, D.-C.; Harding, L. B.; Klippenstein, S. J.; Miller, J. A. *Faraday Discuss.* **2001**, *119*, 207–222.
- (45) MOLPRO is a package of ab initio programs written by H.-J. Werner and P. J. Knowles with contributions from J. Almlof, R. D. Amos, A. Berning, D. L. Cooper, M. J. O. Deegan, A. J. Dobbyn, F. Eckert, S. T. Elbert, Hampel, C.; R. Lindh, A. W. Lloyd, W. Meyer, A. Nicklass, K. Peterson, R. Pitzer, A. J. Stone, P. R. Taylor, M. E. Mura, P. Pulay, M. Schutz, H. Stoll, and T. Thorsteinsson. The majority of calculations reported here were done with Version 2010.1.
- (46) Werner, H.-J.; Knowles, P. J. *J. Chem. Phys.* **1988**, *89*, 5803–5814.
- (47) Knowles, P. J.; Werner, H.-J. *Chem. Phys. Lett.* **1988**, *145*, 514–522.
- (48) Kendall, R. A.; Dunning, T. H., Jr.; Harrison, R. J. *J. Chem. Phys.* **1992**, *96*, 6796–6806.
- (49) Dunning, T. H., Jr. *J. Chem. Phys.* **1989**, *90*, 1007–1023.
- (50) Woon, D. E.; Dunning, T. H., Jr. *J. Chem. Phys.* **1993**, *98*, 1358–1371.
- (51) Werner, H.-J. *Mol. Phys.* **1996**, *89*, 645–661.
- (52) Finley, J.; Malmqvist, P. A.; Roos, B. O. *Chem. Phys. Lett.* **1998**, *288*, 299–306.